Absolute Phase Estimation in Repeat-Pass CSAR Interferometry Based on Backprojection and Split-Bandwidth Techniques

Jianpeng Li, Daoxiang An, *Member, IEEE*, Yongping Song, Junyi Xu, Dong Feng, Leping Chen, *Member, IEEE*, and Zhimin Zhou

***Abstract*—The generation of high-precision ground digital elevation models (DEMs) based on synthetic aperture radar interferometry (InSAR) technology has attracted wide attention. Compared with the linear InSAR technique, the 360° aperture gives circular InSAR (In-CSAR) the capability to generate a full-angle DEM of the observed region. The backprojection (BP) algorithm is considered as a preferred candidate for In-CSAR imaging since it does not impose any restrictions on flight trajectories. After phase unwrapping, a global unknown phase ambiguity exists in the unwrapped phase. Up to now, high-efficient frequency-domain methods, such as the split-bandwidth technique, have commonly been used to estimate the phase ambiguity. However, the split-bandwidth technique cannot be effectively integrated with the BP-focusing image due to the highly nonlinear and nonparallel trajectories of the airborne In-CSAR platforms. We present, for the first time, the combination of BP and split-bandwidth techniques for absolute phase estimation of In-CSAR interferogram in this article. The proposed method can avoid the phase offset induced by split-bandwidth processing under the conditions of highly nonlinear and nonparallel platform trajectories. In addition, the spectral characteristics of the BP-focusing subimage are derived in detail to correct its 2-D space-variant spectral support. In order to reduce the impact of coherence, the weighted least square is adopted to estimate unknown phase ambiguity. The processing results of simulation and real data verify that the proposed approach can effectively estimate the phase ambiguity even under the conditions of highly nonlinear and nonparallel platform trajectories.**

***Index Terms*—Back projection algorithm (BPA), circular synthetic aperture radar interferometry (In-CSAR), split-bandwidth, weighted least square (WLS).**

I. Introduction

IN RECENT years, the technology of synthetic aperture radar interferometry (InSAR) has been developed rapidly [1]. Researchers have made great achievements in the field of data processing. Compared to the high-frequency InSAR system, the repeat-pass low-frequency InSAR system has a larger beam angle and a smaller attenuation. Therefore, the repeat-pass low-frequency InSAR system can generate an accurate digital elevation model (DEM) on a large scale. Unlike conventional SAR from linear trajectories, circular SAR (CSAR) [2] (meaning echo acquired along a circular trajectory), with a high revisit rate, has the ability of a full-angle observation, which makes it possible to obtain a full-angle DEM of the imaging scene. For CSAR interferometry (In-CSAR), three main merits have been exploited. First, compared with the single-angle observation, the multiangle observations of the same target give CSAR the capability to obtain a more accurate DEM. Second, as mentioned in [3], the 360° aperture gives it the capability to detect a hidden target when its orientation is unknown. Third, the multiangle echo of CSAR can reduce the influence of occlusion and shadow while improving the sensitivity of DEM data to topographic relief.

Conventional imaging algorithms are divided into two categories. One is frequency-domain algorithms, such as the range-Doppler (RD) algorithm [4], chirp scaling algorithm [5], and wavenumber domain algorithm [6]. Another is the time-domain algorithm, such as the time-domain backprojection (BP) algorithm [7]. In general, frequency-domain algorithms need to compensate for deviations of the platform trajectory from a linear track. For airborne In-CSAR systems, the deviations mainly include two parts. One is induced by the highly nonlinear circular trajectory of the In-CSAR platform. Another is caused by the influence of airflow. Due to the latter, the airborne platform presents significant time-varying in the forward direction. Therefore, the frequency-domain algorithms require complex motion compensation, which increases the difficulty of SAR imaging. Compared with frequency-domain algorithms, the time-domain BP algorithm can greatly ensure the accuracy of imaging and phase preservation by coherent integration. Moreover, unlike frequency-domain interferometry, time-domain interferometry can be implemented without flattening and removal of topographic phase components [8]. Thus, the BP algorithm is widely used in the field of SAR imaging and interferometry.

One main problem in interferometric processing is the phase ambiguity in the generated interferogram. Determining the

Manuscript received 29 August 2023; revised 16 November 2023; accepted 14 December 2023. Date of publication 25 December 2023; date of current version 8 January 2024. This work was supported in part by the National Natural Science Foundation of China under Grant 42227801, Grant 62271492, Grant 62101562, and Grant 62101566, and in part by the National Natural Science Foundation of China under Grant 61571447. *(Corresponding author: Daoxiang An.)*

Jianpeng Li, Daoxiang An, Yongping Song, Dong Feng, Leping Chen, and Zhimin Zhou are with the College of Electronic Science, National University of Defense Technology, Changsha 410073, China (e-mail: lijianpeng08@163.com; daoxiangan@nudt.edu.cn; sypopqjkl@163.com; fengdong09@nudt.edu.cn; gfkdclp@126.comStudent; zhouzmkd@nudt.edu.cn).

Junyi Xu is with the Aerial Photogrammetry and Remote Sensing Group Company Ltd. of CNACG (ARSC), Xi'an 710000, China (e-mail: junyixu_lm@163.com).

Digital Object Identifier 10.1109/JSTARS.2023.3346950

number of integer phase cycles has been a problem since the first SAR interferograms were formed [9]. In general, the interferometric phase obtained by unwrapping is different from the absolute phase. The unknown constant phase ambiguity can be estimated by the spatial-domain or frequency-domain algorithms. In spatial-domain algorithms, the residual delay estimation (RDE) [10] algorithm is widely used. RDE obtains the residual delay related to phase ambiguity by image registration. However, the complexity of the RDE algorithm increases as the number of estimated values increases. Typical frequency-domain algorithms mainly include split-bandwidth [10], [11], [12] and multichromatic analysis (MCA) [13]. In general, the split-bandwidth algorithm involves two strategies as follows.

- One potential strategy is to execute split-bandwidth processing within the echo domain. First, the raw echo is demodulated to obtain baseband signal. Then, the subband echo is generated by the bandpass filter. Finally, the fullband and subband single look complex subimages (SLCs) are obtained from the echoes of one fullband and two subbands, respectively.
- Another potential strategy is to execute split-bandwidth processing within the image domain. After imaging processing, the spectrum of fullband SLC is split to obtain the lower and upper subband SLCs.

The lower and upper subband SLCs generate the lower and upper subband interferograms. Based on the conjugate multiplication between the lower and upper subband interferograms, both of the abovementioned strategies can generate the double differential interferogram (DDI). In general, the DDI can be used to estimate the unknown phase ambiguity [12]. Compared with the approach in the image domain, the approach in the echo domain introduces greater complexity due to multiple imaging. However, as discussed in [10], the DDI generated from subband echo has a higher accuracy. Unlike the split-band algorithm, MCA uses interferometric pairs of SAR images processed at range subbands and explores the phase trend of each pixel as a function of the different central carrier frequencies to infer absolute optical path differences. However, due to the highly nonlinear and nonparallel trajectories of the airborne In-CSAR platforms, the high-efficient frequency-domain algorithms cannot be effectively integrated with the BP-focusing image.

In this article, for In-CSAR, we quantitatively characterize the interferometric phase of the BP-focusing subimage to estimate the phase ambiguity accurately. On this basis, we propose a novel method of absolute phase estimation, which combines the BP and split-bandwidth techniques. The contributions of the proposed method can be summarized as follows.

1) The 2-D space-variant spectral support of the BP-focusing subimage is corrected by phase compensation. On this basis, the split-bandwidth processing can be correctly implemented on the compensated BP-focusing subimage.
2) Under the conditions of nonlinear and nonparallel trajectories, the DDI is fitted by the unwrapped interferometric phase to avoid the phase offset induced by split-bandwidth processing.
3) To reduce the impact of low coherence region, the weighted least square (WLS) estimation is used to estimate the unknown phase ambiguity.
4) Although the DDI is obtained from the image domain, our proposed method achieves a similar level of estimation accuracy as split-bandwidth processing implemented in the echo domain.

The rest of this article is organized as follows. In Section II, the geometric configuration of In-CSAR and BP focusing technology are presented. We present a novel method of absolute phase estimation based on BP and split-bandwidth techniques in Section III. To examine the validity of our method, the simulation results and analysis are presented in Section IV. The results of absolute phase estimation based on real data are presented in Section V. Finally, Section VI concludes this article.

II. Geometric Configuration of In-CSAR and BP Focusing Technology

A. Geometric Configuration of In-CSAR

The geometric configuration of the repeat-pass In-CSAR system is shown in Fig. 1(a), with the center $\mathbf{O}$ of the imaging scene being defined as the origin of coordinates. The In-CSAR system is equipped on an aircraft and flies along two circular trajectories with radii r_1 and r_2. The heights of the trajectories are denoted by H_1 and H_2, respectively. $\mathbf{B}$ denotes the baseline of the repeat-pass In-CSAR system. For the circular trajectory, the azimuth angle of the radar platform is denoted by φ. Therefore, the instantaneous slant range $R_{\mathrm{c},i}$ from the antenna phase center $\mathbf{P}_{\mathrm{c},i}$ to the point scattering target $\mathbf{A}$ can be expressed as

$$R_{\mathrm{c},i}(\varphi) = \left\|\mathbf{P}_{\mathrm{c},i}(\varphi) - \mathbf{A}\right\|_2, i = 1, 2 \tag{1}$$

where the subscripts $i = 1$ and $i = 2$ represent master and slave trajectories, respectively. $\| \bullet \|_2$ represents the 2-norm, and the stationary target $\mathbf{A}$ is located at (x, y, z). Under the condition of a circular trajectory, the position of the subaperture can be given by

$$\begin{cases} \mathbf{P}_{\mathrm{c},i}(\varphi) = [r_i \cos(\varphi), r_i \sin(\varphi), H_i] \\ \varphi \in (\varphi_0 - \Delta\varphi/2, \varphi_0 + \Delta\varphi/2) \end{cases} \tag{2}$$

where φ_0 is the central azimuth of the subaperture. $\Delta\varphi$ is the integration angle, which is simply referred to as subaperture angle. On account of the symmetry of the flight path, we can rotate the coordinate system with $\mathbf{O}$ as the origin. For the simplicity of carrying out the following analysis, the rotation angle is set to φ_0. Expanding $\mathbf{P}_{\mathrm{c},i}(\varphi)$ into a Taylor series around $\varphi = 0$ yields

$$\begin{cases} \mathbf{P}_{\mathrm{c},i}(\varphi) \approx \left[r_i - \frac{r_i}{2}\varphi^2, r_i\varphi, H_i\right] \\ \varphi \in (-\Delta\varphi/2, \Delta\varphi/2). \end{cases} \tag{3}$$

After rotation, the *X*-axis and *Y*-axis directions of a Cartesian coordinate system represent the ground range and azimuth directions, respectively. Affected by airflow, the actual trajectory of the platform usually deviates from the ideal trajectory, as illustrated in Fig. 1(b). In such cases, the actual master and slave trajectories are represented by the black and red curves, respectively. The ideal trajectory is represented by a blue dashed

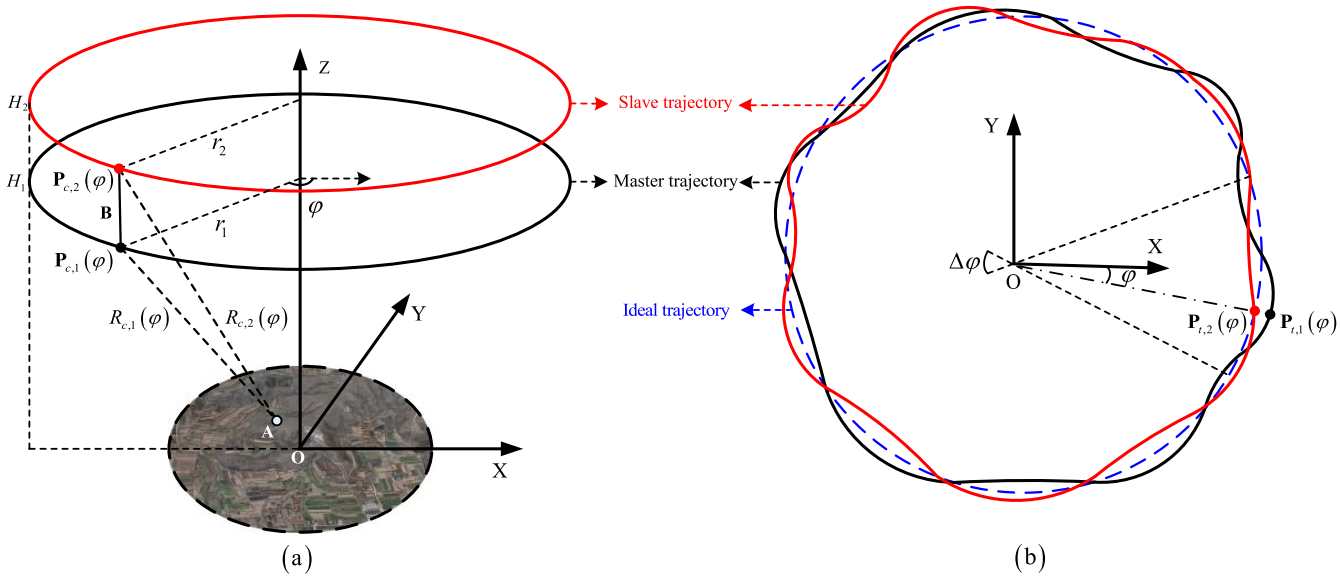

Fig. 1. Geometric configuration of the repeat-pass L-band In-CSAR system. (a) Side view. (b) Corresponding top view. Typically, airborne platforms struggle to maintain ideal circular motion.

line. Therefore, the true position $\mathbf{P}_{\mathrm{t},i}$ of the subaperture can be expressed as

$$\mathbf{P}_{\mathrm{t},i}(\varphi) \approx \mathbf{P}_{\mathrm{c},i}(\varphi) + \mathbf{P}_{\mathrm{e},i}(\varphi) \tag{4}$$

where $\mathbf{P}_{\mathrm{e},i}$ is the error between the actual and ideal trajectories. Expanding $\mathbf{P}_{\mathrm{e},i}(\varphi)$ into a Taylor series around $\varphi = 0$ in the spatial coordinate system yields

$$\begin{aligned}\mathbf{P}_{e,i}(\varphi) &= \boldsymbol{\sigma}_i \left[1, \varphi, \varphi^2\right]^T + O(\varphi) \\ &= \begin{bmatrix} \sigma_{x_0,i} & \sigma_{x_1,i} & \sigma_{x_2,i} \\ \sigma_{y_0,i} & \sigma_{y_1,i} & \sigma_{y_2,i} \\ \sigma_{z_0,i} & \sigma_{z_1,i} & \sigma_{z_2,i} \end{bmatrix} \begin{bmatrix} 1 \\ \varphi \\ \varphi^2 \end{bmatrix} + O(\varphi)\end{aligned} \tag{5}$$

where $\boldsymbol{\sigma}_i$ is the coefficient matrix. $O(\varphi)$ is the summation of the higher order terms ($\geq$2nd).

B. BP Focusing Technology

Due to the time-variant line-of-sight (LOS) of In-CSAR, the ground range SAR image is obtained by the time-domain imaging algorithm. A brief derivation of the time-domain BP algorithm is given in this section.

The linear frequency modulation signal is used as the transmitted signal. After demodulation and pulse compression, the echo S_i of target $\mathbf{A}$ echo is modeled as

$$S_i(t,\varphi) = \mathrm{sinc}\left\{B_{\mathrm{r}}\left[t - \frac{2R_{\mathrm{t},i}(\varphi)}{c}\right]\right\} \exp\left[-jk_{\mathrm{c}}R_{\mathrm{t},i}(\varphi)\right] \tag{6}$$

where $\mathrm{sinc}(x) = \sin(\pi x)/(\pi x)$. t and c are the fast time and the speed of light, respectively. B_r and k_c are the bandwidth and wavenumber, respectively. The instantaneous slant range $R_{\mathrm{t},i}(\varphi) = \|\mathbf{P}_{\mathrm{t},i}(\varphi) - \mathbf{A}\|_2$. The most important step for the BP algorithm is coherent superposition of contributions from each pulse. Suppose that the target $\mathbf{A}$ is focused near pixel $\mathbf{A}'$. Therefore, the correction function generated by the distance between the pixel $\mathbf{A}'$ and the radar platform is used to compensate the phase component in (6). After coherent superposition, the backprojected signal of the target $\mathbf{A}$ can be expressed as

$$I_i = \int_{\varphi} S_i(t,\varphi) \exp\left(jk_{\mathrm{c}}\|\mathbf{P}_{\mathrm{t},i}(\varphi) - \mathbf{A}'\|_2\right) d\varphi. \tag{7}$$

The stationary pixel $\mathbf{A}'$ is located at (x', y', z'). Substituting (6) into (7), we can obtain

$$I_i = \int_{\varphi} \mathrm{sinc}\left[\frac{2B_{\mathrm{r}}}{c}\Delta R_i(\varphi)\right] \exp\left[jk_{\mathrm{c}}\Delta R_i(\varphi)\right] d\varphi \tag{8}$$

where $\Delta R_i(\varphi) = \|\mathbf{P}_{\mathrm{t},i}(\varphi) - \mathbf{A}'\|_2 - \|\mathbf{P}_{\mathrm{t},i}(\varphi) - \mathbf{A}\|_2$. Expanding the range difference $\Delta R_i(\varphi)$ into a second-order Taylor series, we have

$$\Delta R_i(\varphi) \approx \Delta R_{i,0} + \Delta R_{i,1}\varphi + \Delta R_{i,2}\varphi^2 \tag{9}$$

where

$$\begin{cases} \Delta R_{i,0} = \|\mathbf{P}_{\mathrm{t},i}(\varphi) - \mathbf{A}'\|_2 - \|\mathbf{P}_{\mathrm{t},i}(\varphi) - \mathbf{A}\|_2 \\ \Delta R_{i,1} \approx \frac{\boldsymbol{\sigma}_{1,i}\cdot(\mathbf{A}-\mathbf{A}')}{\|\mathbf{P}_{\mathrm{t},i}(\varphi)-\mathbf{A}'\|_2} \\ \Delta R_{i,2} \approx \frac{\boldsymbol{\sigma}_{2,i}\cdot(\mathbf{A}-\mathbf{A}')}{2\|\mathbf{P}_{\mathrm{t},i}(\varphi)-\mathbf{A}'\|_2} \end{cases} \tag{10}$$

where $(\cdot)$ is the dot product. The vector $\boldsymbol{\sigma}_{1,i}$ and $\boldsymbol{\sigma}_{2,i}$ can be expressed as

$$\begin{cases} \boldsymbol{\sigma}_{1,i} = [\sigma_{x_1,i}, \sigma_{y_1,i} + r_i, \sigma_{z_1,i}] \\ \boldsymbol{\sigma}_{2,i} = [2\sigma_{x_2,i} + r_i, 2\sigma_{y_2,i}, 2\sigma_{z_2,i}]. \end{cases} \tag{11}$$

Obviously, the vectors $\boldsymbol{\sigma}_{1,i}$ and $\boldsymbol{\sigma}_{2,i}$ are related to the velocity and shape of the subaperture, respectively. Substituting (9) into (8), we can obtain

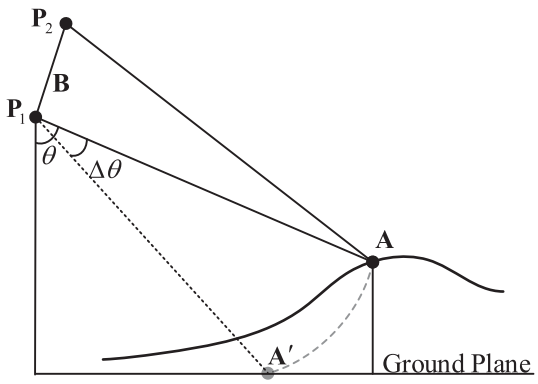

Fig. 2. Imaging geometry of a single subaperture based on In-CSAR. Points $\mathbf{A}'$ and $\mathbf{A}$ are the physical center of the pixel and the actual phase center of a scattering target, respectively. Obviously, the vector $\mathbf{P}_1\mathbf{A}$ and vector $\mathbf{P}_1\mathbf{A}'$ lie in the same Doppler plane.

$$I_i \approx \Delta\varphi \int_{\varphi} \operatorname{sinc}\left[\frac{2B_{\mathrm{r}}}{c}\Delta R_i(\varphi)\right] \exp\left[jk_{\mathrm{c}}\left(\Delta R_{i,1}\varphi\right)\right] d\varphi \times \exp\left[jk_{\mathrm{c}}\left(\Delta R_{i,0}+\Delta R_{i,2}\frac{\Delta\varphi^2}{12}\right)\right]. \tag{12}$$

We can see from (12) that the focusing position of the target is determined by the two terms in the integral sign. In addition to constant and quadratic components of the range difference ΔR_i, the linear component can also shift the position of the impulse response. The phase is determined by the last term in (12). Thus, the constant and quadratic components of the range difference induce a phase offset. For In-CSAR model, the phase center $\mathbf{P}_i$ of the subaperture is given as

$$\begin{aligned}\mathbf{P}_i &= [X_i, Y_i, Z_i] \\ &\approx \begin{bmatrix} r_i + \sigma_{x_0,i} + (2\sigma_{x_2,i} - r_i)\Delta\varphi^2/24 \\ \sigma_{y_0,i} + \sigma_{y_2,i}\Delta\varphi^2/12 \\ H_i + \sigma_{z_0,i} + \sigma_{z_2,i}\Delta\varphi^2/12 \end{bmatrix}^T.\end{aligned} \tag{13}$$

Corresponding to (11), the equivalent velocity $\mathbf{V}_i$ of the subaperture can be expressed as

$$\begin{aligned}\mathbf{V}_i &= [V_{x,i}, V_{y,i}, V_{z,i}] \\ &\approx \left[\frac{\sigma_{x_1,i}\varphi}{t_{\mathrm{a}}}, \frac{[\sigma_{y_1,i} + r_i]\,\varphi}{t_{\mathrm{a}}}, \frac{\sigma_{z_1,i}\varphi}{t_{\mathrm{a}}}\right]\end{aligned} \tag{14}$$

where t_{a} is the slow time of subaperture. The location algorithm of airborne SAR image based on RD model can be expressed as

$$\begin{cases} \|\mathbf{P}_i - \mathbf{A}\|_2 \approx \|\mathbf{P}_i - \mathbf{A}'\|_2 \\ \mathbf{V}_i \cdot (\mathbf{P}_i - \mathbf{A}) \approx \mathbf{V}_i \cdot (\mathbf{P}_i - \mathbf{A}'). \end{cases} \tag{15}$$

Therefore, the imaging geometry of a single subaperture based on In-CSAR is shown in Fig. 2. θ and $\Delta\theta$ are the incidence angle and differential incidence angle, respectively. Substituting (13)–(15) into (12), the BP-focusing subimage in the ground-range plane can be expressed as

$$I_i = \operatorname{sinc}\left[\beta_y\left(y' - y + \Delta y_i\right)\right] \operatorname{sinc}\left[\beta_x\left(x' - x + \Delta x_i\right)\right] \times \exp\left[jk_{\mathrm{c}}\left(\|\mathbf{P}_i - \mathbf{A}'\|_2 - \|\mathbf{P}_i - \mathbf{A}\|_2\right)\right] \tag{16}$$

where β_y is the azimuth resolution. β_x is the ground-range resolution. Given (16), the relationship between the azimuth offset Δy_i or range offset Δx_i and the real DEM can be approximated by

$$\begin{cases} \Delta y_i = \zeta_{y,i}(z - z') \\ \quad \approx \dfrac{\left(Z_i - \dfrac{z'+z}{2}\right)V_{x,i} - \left(X_i - \dfrac{x'+x}{2}\right)V_{z,i}}{\left(Y_i - \dfrac{y'+y}{2}\right)V_{x,i} - \left(X_i - \dfrac{x'+x}{2}\right)V_{y,i}}(z - z') \\ \Delta x_i = \zeta_{x,i}(z - z') \\ \quad \approx \dfrac{\left(Z_i - \dfrac{z'+z}{2}\right)V_{y,i} - \left(Y_i - \dfrac{y'+y}{2}\right)V_{z,i}}{\left(X_i - \dfrac{x'+x}{2}\right)V_{y,i} - \left(Y_i - \dfrac{y'+y}{2}\right)V_{x,i}}(z - z'). \end{cases} \tag{17}$$

We can see that the coefficients $\zeta_{y,i}$ and $\zeta_{x,i}$ not only rely on the real DEM but also depend on the velocity vectors and phase centers of subapertures. Therefore, the position of impulse response is related to the position and velocity of the subaperture. To perform split-bandwidth processing correctly, it is necessary to quantitatively characterize the 2-D spectral support of fullband subimage. The 2-D Fourier transform (FT) D_i of the BP-focusing subimage can be expressed as

$$D_i = \iint_{x',y'} I_i \exp\left[-j\left(k_{x'}x' + k_{y'}y'\right)\right] dx'dy'. \tag{18}$$

We find that the position of the 2-D spectral support is related to the position of the point target. Unlike the spectrum of the echo S_i, the spectral support of the BP-focusing subimage I_i is 2-D space-variant [14]. Therefore, an additional phase compensation is needed before split-bandwidth in the image domain. For the BP-focusing subimage, the exponential term generated by the pixel $\mathbf{A}'$ must be corrected. After phase compensation, the compensated subimage $I_{\mathrm{c},i}$ can be expressed as

$$\begin{aligned} I_{\mathrm{c},i} &= I_i \times S_{\mathrm{cor},i} \\ &= \operatorname{sinc}\left[\beta_y\left(y' - y + \Delta y_i\right)\right] \operatorname{sinc}\left[\beta_x\left(x' - x + \Delta x_i\right)\right] \\ &\quad \times \exp\left(-jk_{\mathrm{c}}\|\mathbf{P}_i - \mathbf{A}\|_2\right) \end{aligned} \tag{19}$$

where the correction function $S_{\mathrm{cor},i} = \exp(-jk_{\mathrm{c}}\|\mathbf{P}_i - \mathbf{A}'\|_2)$ generated from the phase center $\mathbf{P}_i$ of nonlinear subaperture and the position of the pixel $\mathbf{A}'$. From (13), the phase center $\mathbf{P}_i$ can be estimated by the true position of the subaperture. Corresponding to (18), the 2-D FT $D_{\mathrm{c},i}$ of the subimage $I_{\mathrm{c},i}$ can be expressed as

$$\begin{aligned} D_{\mathrm{c},i} \approx \frac{1}{\beta_y\beta_x}&\operatorname{rect}\left(\frac{k_{y'}}{2\pi\beta_y}\right)\operatorname{rect}\left(\frac{k_{x'}}{2\pi\beta_x}\right) \\ &\times \exp\left(-jk_{\mathrm{c}}\|\mathbf{P}_i - \mathbf{A}\|_2\right) \\ &\times \exp\left[-jk_{y'}\left(y - \Delta y_i\right) - jk_{x'}\left(x - \Delta x_i\right)\right] \end{aligned} \tag{20}$$

where rect(•) means the rectangle window. We can see from (20) that the 2-D space-variant spectral support of the subimage has been corrected. Thus, the split-bandwidth processing

can be correctly implemented on the compensated BP-focusing subimage $I_{c,i}$. After InSAR processing, the interferogram Q_c^F of fullband subimage can be expressed as

$$\begin{aligned} Q_c^F &= I_{c,1} \cdot (I_{c,2})^* \\ &= \text{sinc}\left[\beta_y\left(y' - y + \Delta y_1\right)\right] \text{sinc}\left[\beta_x\left(x' - x + \Delta x_1\right)\right] \\ &\quad \times \exp\left[jk_c\left(\|\mathbf{P}_2 - \mathbf{A}\|_2 - \|\mathbf{P}_1 - \mathbf{A}\|_2\right)\right] \\ &\quad \times \exp\left[jk_c\left(\|\mathbf{P}_1 - \mathbf{A}'\|_2 - \|\mathbf{P}_2 - \mathbf{A}'\|_2\right)\right] \end{aligned} \tag{21}$$

where $(\bullet)^*$ is the conjugate operation. The unwrapping operation is performed on the fullband interferogram Q_c^F to obtain unwrapped phase Φ_{unw}. Due to the phase ambiguity, the unwrapped phase Φ_{unw} of the fullband interferogram Q_c^F can be expressed as

$$\begin{aligned} \Phi_{unw} &= \text{unwrap}(\angle Q_c^F) \\ &= k_c\left(\|\mathbf{P}_2 - \mathbf{A}\|_2 - \|\mathbf{P}_1 - \mathbf{A}\|_2\right) \\ &\quad + k_c\left(\|\mathbf{P}_1 - \mathbf{A}'\|_2 - \|\mathbf{P}_2 - \mathbf{A}'\|_2\right) - \Phi_{amb} \end{aligned} \tag{22}$$

where $\text{unwrap}(\bullet)$ is the unwrapping operation. $\Phi_{amb} = 2n\pi$ is the phase ambiguity. n is an unknown integer. We can see from (22) that the flat-Earth phase $k_c(\|\mathbf{P}_2 - \mathbf{A}'\|_2 - \|\mathbf{P}_1 - \mathbf{A}'\|_2)$ is removed. From (21), the absolute phase Φ_{abs} can be approximately expressed as

$$\Phi_{abs} \approx 2k_c \frac{(\mathbf{A} - \mathbf{A}') \cdot (\mathbf{P}_1 - \mathbf{P}_2)}{\|\mathbf{P}_1 - \mathbf{A}'\|_2 + \|\mathbf{P}_2 - \mathbf{A}'\|_2}. \tag{23}$$

Substituting (23) into (22), the relationship between the unwrapped phase Φ_{unw} and the absolute phase Φ_{abs} can be expressed as

$$\Phi_{unw} = \Phi_{abs} - \Phi_{amb}. \tag{24}$$

To enhance the precision of DEM, an accurate estimation of the unknown integer n is required after the unwrapping operation.

III. Absolute Phase Estimation in Repeat-Pass In-CSAR

A. Split-Bandwidth Processing

For InSAR, the phase ambiguity is needed to compensate for deviations of the unwrapped phase from the absolute phase. In general, the high-efficient split-bandwidth technique [10], [11], [12] can estimate the phase ambiguity effectively.

The split-bandwidth processing based on the BP-focusing subimage is shown in Fig. 3. $\pm\Delta k$ are the upper and lower subband positions of the subimages, respectively. The available range bandwidth is $2\pi\beta_x$ and the width of the subband is $2\pi\alpha\beta_x$. α is the subband-to-fullband ratio. The error standard deviation σ_{split} of the split-bandwidth estimator can be expressed as [15]

$$\sigma_{split} \frac{1}{2} \frac{1}{1-\alpha} \sqrt{\frac{1}{\alpha} \frac{1}{\sqrt{M}} \frac{\sqrt{1-\gamma^2}}{\pi\gamma}} \tag{25}$$

where γ denotes the coherence. M is the number of useful pixels. From (25), as M increases, the robustness of the split-bandwidth estimator increases. The standard deviation of the split-bandwidth estimator is dependent on both subband location

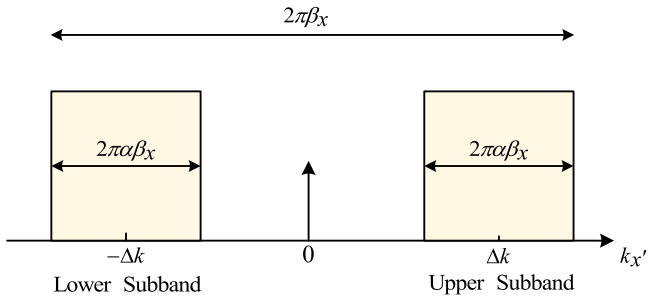

Fig. 3. Bandpass filtering of the fullband subimages based on split-bandwidth technique.

and bandwidth [9], [15]. For two subbands, the standard deviation is minimized when the subband-to-fullband ratio $\alpha = 1/3$. In addition, the centers of the subbands are $\pm B_r/3$ away from the center of the fullband. Thus, in this article, the optimal subband bandwidth $B_r/3$ is used to process both simulated and real data.

First, the fullband SLCs of master and slave subapertures are generated. Then, each of the master and slave SLCs is split into a lower and an upper subband SLC. In addition, the lower and upper subband interferograms are obtained by the lower and the upper subband SLCs, respectively. Finally, the two subband interferograms are used to generate a DDI. In the registration processing, the subband image needs to be resampled. However, the interpolating function used for resampling should be an ideal low-pass filter [21]. To obtain baseband signal and improve the accuracy of registration, the spectrum shifting (i.e., demodulation) and lowpass filtering are used to replace the bandpass filtering of split-bandwidth processing in this article. The 2-D FT $D_{c,i}^L$ and $D_{c,i}^U$ of subband subimages based on In-CSAR system can be expressed as

$$\begin{cases} D_{c,i}^L = \mathbf{F}(D_{c,i}) \exp\left[-j\Delta k\left(x - \Delta x_i\right)\right] \\ D_{c,i}^U = \mathbf{F}(D_{c,i}) \exp\left[+j\Delta k\left(x - \Delta x_i\right)\right] \end{cases} \tag{26}$$

where $\mathbf{F}(\cdot)$ is the lowpass filtering operation. The superscripts L and U represent the lower subband and upper subband, respectively. As we know, the range resolution is related to the bandwidth. Thus, the split-bandwidth processing reduces the range resolution. However, compared to the changes in resolution, the phase changes are more worthy of attention. Consequently, the relationship between the subband and the fullband SLCs is

$$\begin{cases} I_{c,i}^L \approx I_{c,i} \exp\left[-j\Delta k\left(x - \Delta x_i\right)\right] \\ I_{c,i}^U \approx I_{c,i} \exp\left[+j\Delta k\left(x - \Delta x_i\right)\right] \end{cases} \tag{27}$$

where $I_{c,i}^L$ and $I_{c,i}^U$ represent the lower subband SLCs and the upper subband SLCs, respectively. After InSAR processing, the lower and upper subband interferograms can be expressed as

$$\begin{cases} Q_c^L = I_{c,1}^L \cdot \left(I_{c,2}^L\right)^* \approx Q_c^F \exp\left[-j\Delta k\left(\Delta x_2 - \Delta x_1\right)\right] \\ Q_c^U = I_{c,1}^U \cdot \left(I_{c,2}^U\right)^* \approx Q_c^F \exp\left[+j\Delta k\left(\Delta x_2 - \Delta x_1\right)\right]. \end{cases} \tag{28}$$

Based on (28), in order to estimate the absolute phase, the DDI Q_c^{diff} generated by the two subband interferograms can

be obtained as

$$\begin{aligned} Q_{\mathrm{c}}^{\mathrm{diff}} &= Q_{\mathrm{c}}^{\mathrm{L}} \cdot \left(Q_{\mathrm{c}}^{\mathrm{U}}\right)^{*} \\ &= \operatorname{sinc}\left[\beta_y\left(y'-y+\Delta y_1\right)\right] \operatorname{sinc}\left[\alpha\beta_x\left(x'-x+\Delta x_1\right)\right] \\ &\quad \times \exp\left[-j2\Delta k\left(\Delta x_2-\Delta x_1\right)\right]. \end{aligned} \tag{29}$$

To make the comparison, it is necessary to derive the expression of the DDI based on the echo domain. Corresponding to (16), the DDI $Q_{\mathrm{echo}}^{\mathrm{diff}}$ based on subband echo can be expressed as

$$\begin{aligned} Q_{\mathrm{echo}}^{\mathrm{diff}} &= \operatorname{sinc}\left[\beta_y\left(y'-y+\Delta y_1\right)\right] \operatorname{sinc}\left[\alpha\beta_x\left(x'-x+\Delta x_1\right)\right] \\ &\quad \times \exp\left[j2\Delta k\left(\|\mathbf{P}_1-\mathbf{A}\|_2-\|\mathbf{P}_2-\mathbf{A}\|_2\right)\right] \\ &\quad \times \exp\left[j2\Delta k\left(\|\mathbf{P}_2-\mathbf{A}'\|_2-\|\mathbf{P}_1-\mathbf{A}'\|_2\right)\right]. \end{aligned} \tag{30}$$

From (21) and (30), it can be seen that the terrain phase of $Q_{\mathrm{echo}}^{\mathrm{diff}}$ is proportional to the phase of $Q_{\mathrm{c}}^{\mathrm{F}}$. Comparison of (29) with (30) indicates that the phase of $Q_{\mathrm{echo}}^{\mathrm{diff}}$, which is derived from echo domain, remains independent of the velocity of the platform. Therefore, the relationship between $Q_{\mathrm{c}}^{\mathrm{diff}}$ and $Q_{\mathrm{echo}}^{\mathrm{diff}}$ can be expressed as

$$\begin{cases} Q_{\mathrm{c}}^{\mathrm{diff}} \approx Q_{\mathrm{echo}}^{\mathrm{diff}} \\ \text{s.t. } V_{x,i}=V_{z,i}=0. \end{cases} \tag{31}$$

From (21) and (31), we can see that the nonparallel trajectories have disrupted the proportional relationship between $Q_{\mathrm{c}}^{\mathrm{diff}}$ and $Q_{\mathrm{c}}^{\mathrm{F}}$. This means that the nonparallel trajectories of the platform induce a phase offset in the DDI $Q_{\mathrm{c}}^{\mathrm{diff}}$. Therefore, the split-bandwidth technique cannot be effectively integrated with the BP-focusing image.

B. Novel Method of Absolute Phase Estimation

As mentioned previously, there is a phase offset in the DDI $Q_{\mathrm{c}}^{\mathrm{diff}}$. To avoid this phase offset, the unwrapped phase of fullband interferogram $Q_{\mathrm{c}}^{\mathrm{F}}$ is used to fit the DDI $Q_{\mathrm{c}}^{\mathrm{diff}}$ in this article. Obviously, the fitting error is minimized when $\Phi_{\mathrm{amb}}=0$. The relationship between absolute DEM h_{abs} and the absolute phase can be expressed as [16]

$$\begin{aligned} h_{\mathrm{abs}} &= z-z' \\ &\approx \Phi_{\mathrm{abs}} \frac{\|\mathbf{P}_1-\mathbf{A}'\|_2+\|\mathbf{P}_2-\mathbf{A}'\|_2}{2k_{\mathrm{c}}\left[B_{\parallel}/\tan\left(\theta-\Delta\theta/2\right)+B_{\perp}\right]} \end{aligned} \tag{32}$$

where $B_{\parallel}$ and $B_{\perp}$ are the horizontal and vertical components of the baseline $\mathbf{B}$ in the Cartesian coordinates, respectively. However, the phase ambiguity is unknown. From (24), without absolute phase determination, the DEM h_{unw} generated by the unwrapped phase can be expressed as

$$h_{\mathrm{unw}} = h_{\mathrm{abs}} - h_{\mathrm{amb}} \tag{33}$$

where h_{amb} is the DEM ambiguity induced by the phase ambiguity. In general, the differential interferometric phase is related to the velocity and position of the subapertures. Substituting (17) into (29), the differential interferometric phase $\Phi_{\mathrm{f}}^{\mathrm{diff}}$ fitted by the DEM h_{unw} can be expressed as

$$\Phi_{\mathrm{f}}^{\mathrm{diff}} = 2\Delta k(\hat{\zeta}_{x,1}-\hat{\zeta}_{x,2})h_{\mathrm{unw}} \tag{34}$$

where $\hat{\zeta}_{x,1}$ and $\hat{\zeta}_{x,2}$ are the estimated values of the coefficients. Substituting the DEM h_{unw}, $\mathbf{V}_i$ and $\mathbf{P}_i$ into (17), the estimations of the coefficients $\hat{\zeta}_{x,1}$ and $\hat{\zeta}_{x,2}$ can be obtained. Based on the absolute DEM h_{abs}, the true differential interferometric phase $\Phi_{\mathrm{c}}^{\mathrm{diff}}$ of the DDI $Q_{\mathrm{c}}^{\mathrm{diff}}$ can be expressed as

$$\Phi_{\mathrm{c}}^{\mathrm{diff}} = 2\Delta k(\zeta_{x,1}-\zeta_{x,2})h_{\mathrm{abs}}. \tag{35}$$

Based on (34) and (35), to estimate the phase ambiguity, the differential phase $\Delta\Phi$ for the $\Phi_{\mathrm{c}}^{\mathrm{diff}}$ and $\Phi_{\mathrm{f}}^{\mathrm{diff}}$ can be obtained as

$$\begin{aligned} \Delta\Phi &= \Phi_{\mathrm{c}}^{\mathrm{diff}} - \Phi_{\mathrm{f}}^{\mathrm{diff}} \\ &= 2\Delta k(\hat{\zeta}_{x,1}-\hat{\zeta}_{x,2})h_{\mathrm{amb}} - 2\Delta k\Delta\zeta h_{\mathrm{abs}} \end{aligned} \tag{36}$$

where $\Delta\zeta=(\hat{\zeta}_{x,1}-\hat{\zeta}_{x,2})-(\zeta_{x,1}-\zeta_{x,2})$ is the error of the coefficient. Under the condition of $Z_i \gg h_{\mathrm{amb}}$, we have $\Delta\zeta\approx 0$. In order to reduce the impact of coherence, the number of phase ambiguity $\hat{n}$ can be obtained by the WLSs estimation as

$$\hat{n} = \operatorname{round}\left[\frac{(\mathbf{\Lambda}^T\mathbf{W}\mathbf{\Lambda})^{-1}\mathbf{\Lambda}^T\mathbf{W}\Delta\Phi}{2\pi}\right] \tag{37}$$

where

$$\mathbf{\Lambda} = \frac{\Delta k(\hat{\zeta}_{x,1}-\hat{\zeta}_{x,2})\left(\|\mathbf{P}_1-\mathbf{A}'\|_2+\|\mathbf{P}_2-\mathbf{A}'\|_2\right)}{k_{\mathrm{c}}\left[B_{\parallel}/\tan\left(\theta-\Delta\theta/2\right)+B_{\perp}\right]} \tag{38}$$

where $\mathbf{W}$ denotes a $M\times M$ weighting matrix. In the case of uncorrelated noise, the form of $\mathbf{W}$ can expressed as

$$\mathbf{W} = \operatorname{diag}\left\{\frac{1}{\sigma_1^2},\frac{1}{\sigma_2^2},\ldots,\frac{1}{\sigma_M^2}\right\} \tag{39}$$

where σ_m denotes the standard deviation of the differential phases $\Delta\Phi$.

After WLS estimation, the fitted phase $\Phi_{\mathrm{f}}^{\mathrm{diff}}$ can be updated to reduce the error of the coefficient $\Delta\zeta$. Based on (36), in order to improve the accuracy of estimation, the iterative algorithm is used to correct the estimated values $\hat{\zeta}_{x,1}$ and $\hat{\zeta}_{x,2}$. If the previous and subsequent estimated results are the same, the iteration will be stopped. Thus, the termination condition of the iteration is that the estimated value $\hat{n}$ no longer changes. Fig. 4 shows the flowchart of the proposed method. The procedure to perform the absolute phase estimation in this article can be listed as follows.

Step 1: Preprocessing is necessary for the BP-focusing subimage. The phase compensation function is used to correct the 2-D space-variant spectral support of the BP-focusing subimage.

Step 2: The split-bandwidth processing is carried out. The fullband subimage is split into the lower and upper subband subimages. Then, the differential interferogram is obtained.

Step 3: The preunwrapping-assisted minimum discontinuity (PAMD) phase-unwrapping method is used to obtain the unwrapped interferometric phase of the fullband subimage [25].

Step 4: The absolute phase estimation is preformed. The differential interferometric phase is fitted by the unwrapped interferometric phase. The unknown phase ambiguity can be estimated by WLS estimation.

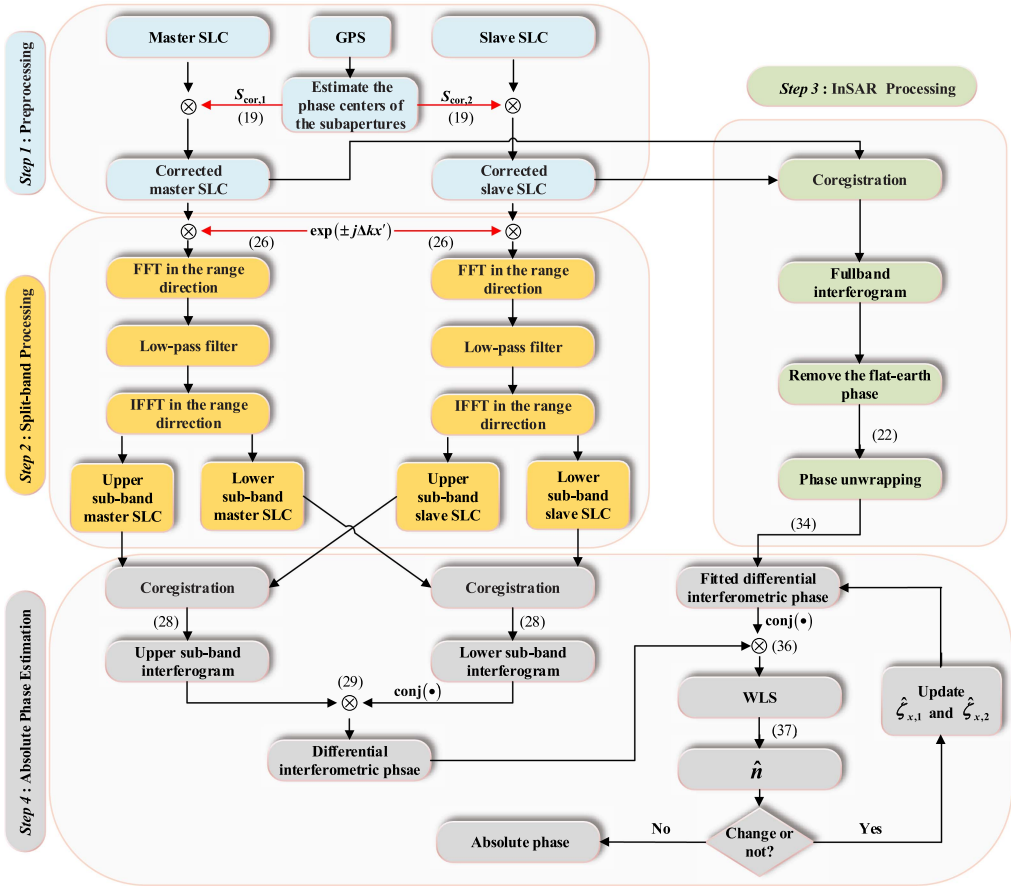

Fig. 4. Flowchart of absolute phase estimation using the BP-based split-bandwidth technique. For ground range BP-focusing images, the preliminary geometric registration of the master and slave subimages has been completed. To achieve high-precision registration, the incoherent speckle correlation [15] is used to improve the accuracy of registration.

TABLE I
IMAGING PARAMETERS OF REPEAT-PASS CIRCULAR INSAR

Parameter name	Values
Carrier frequency	L band
Bandwidth-to-frequency ratio	0.16
Height of the master trajectory	2000 m
Height of the slave trajectory	2030 m
Radius of the master trajectory	2000 m
Radius of the slave trajectory	1990 m
Equivalent velocity of the master subaperture	$(0, 100, 0)$ m/s
Equivalent velocity of the slave subaperture	$(10, 100, 0)$ m/s
Azimuth of the subaperture	0 rd
Integration angle of the subaperture	0.3 rd
Height of the cone	100 m
Radius of the cone	600 m
Size of the imaging scene	1600 m $\times$ 1600 m
Signal to noise ratio	3 dB

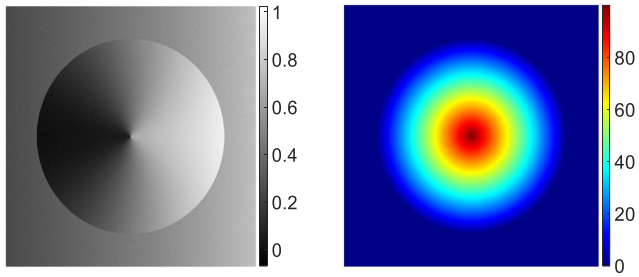

Fig. 5. Imaging scene in the original DEM geometry. (a) Scattering coefficients. (b) Real DEM data (unit: m).

IV. SIMULATION RESULTS AND ANALYSIS

A. Result of InSAR Processing

In this section, the effectiveness and practicability of the proposed approach are verified with the processing results of simulation data. The main parameters involved in the simulations are given in Table I. For repeat-pass L-band system, to ensure InSAR measurement accuracy and coherence, the horizontal and vertical components of the baseline $\mathbf{B}$ are 10 and –30 m, respectively. In the interferometric phase, the noise is assumed to be additive white Gaussian noise at a level of 3 dB.

Due to the time-variant LOS of In-CSAR, the ground range SAR image is obtained in the original DEM geometry. The scattering coefficients and DEM of the imaging scene are shown in Fig. 5(a) and (b), respectively. The scattering coefficients of the imaging scene are calculated from the incidence angle. As shown in Fig. 5(b), the center of the cone coincides with the

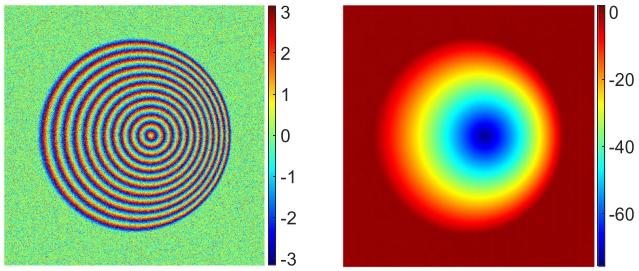

Fig. 6. Interferometric results of the fullband subimage in the original DEM geometry (unit: rad). (a) Interferometric phase without flat-Earth phase. (b) Unwrapped phase.

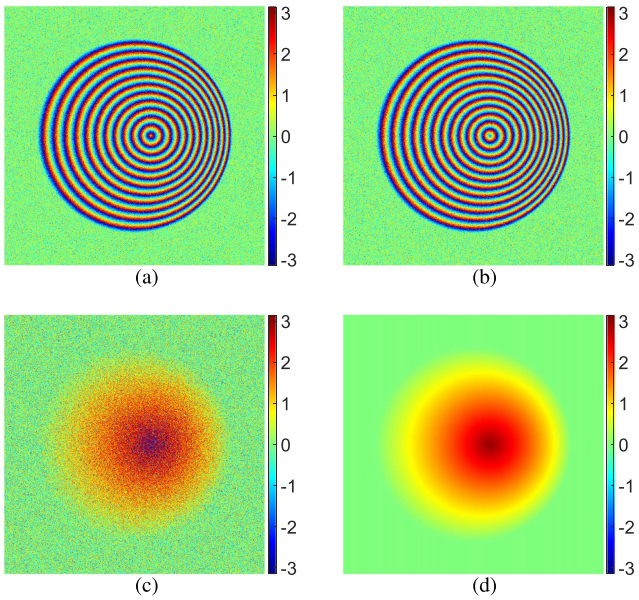

Fig. 7. Result of split-bandwidth in the echo domain (unit: rad). (a) Lower subband interferometric phase. (b) Upper subband interferometric phase. (c) Real differential interferometric phase. (d) Fitted differential interferometric phase based on the proposed method.

center of the imaging scene. It is assumed that a horizontal reference plane is used for BP imaging without external DEM assistance. After coregistration and flat-Earth phase removal, the interferometric phase of the fullband subimage is shown in Fig. 6(a). Based on the PAMD phase-unwrapping method, the unwrapped phase is obtained. The unwrapped phase is shown in Fig. 6(b). Comparison of Fig. 5(b) with Fig. 6(b) indicates that the terrain height can induce a range offset in the BP-focusing subimage.

In order to evaluate the accuracy of the proposed algorithm, the split-bandwidth processing was performed in the echo domain and image domain, respectively.

B. Result of Split-Bandwidth in Echo Domain

The lower and upper subband interferometric phases obtained by the split-bandwidth processing in the echo domain are shown in Fig. 7(a) and (b), respectively. Correspondingly, the real differential interferometric phase for the lower and upper interferograms is shown in Fig. 7(c). The ratio of the carrier frequency to the frequency difference between lower and upper interferograms (i.e., $k_c/2\Delta k$) is about 25. Obviously, the split-bandwidth technique can reduce the number of interference fringes. Thus, the absolute phase without ambiguity can be generated by split-bandwidth technique. Comparison of Fig. 6(b) with Fig. 7(c) indicates that the terrain phase is proportional to the differential interferometric phase obtained by split-bandwidth processing in the echo domain. After absolute phase determination and phase filtering, the fitted differential interferometric phase is shown in Fig. 7(d). The phase error between the real and fitted differential interferometric phases is shown in Fig. 9(a). The variance of phase error is 0.0017 rad.

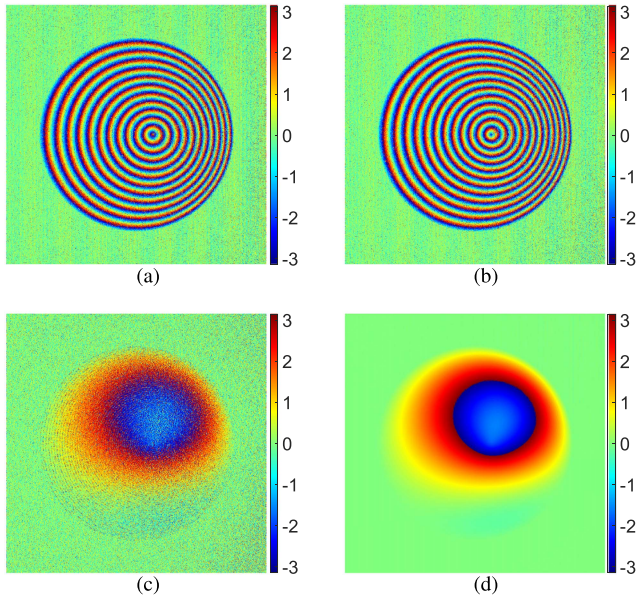

Fig. 8. Result of split-bandwidth in the BP-focusing image domain (unit: rad). (a) Lower subband interferometric phase. (b) Upper subband interferometric phase. (c) Real differential interferometric phase. (d) Fitted differential interferometric phase based on the proposed method.

C. Result of Split-Bandwidth in BP-Focusing Image Domain

The lower and upper subband interferometric phases generated by split-bandwidth processing in the BP-focusing image domain are shown in Fig. 8(a) and (b), respectively. Correspondingly, the real differential interferometric phase obtained by split-bandwidth processing in the BP-focusing image domain is shown in Fig. 8(c). Comparison of Fig. 7(c) with Fig. 8(c) indicates that the phase offset is induced by the nonparallel trajectories of the platform. Therefore, the difference in velocity vectors between the master and slave subapertures will affect the split-bandwidth processing based on the image domain. After absolute phase determination, the fitted differential interferometric phase is shown in Fig. 8(d). The phase error between the real and fitted differential interferometric phases is shown in Fig. 9(b). The variance of phase error is 0.003 rad.

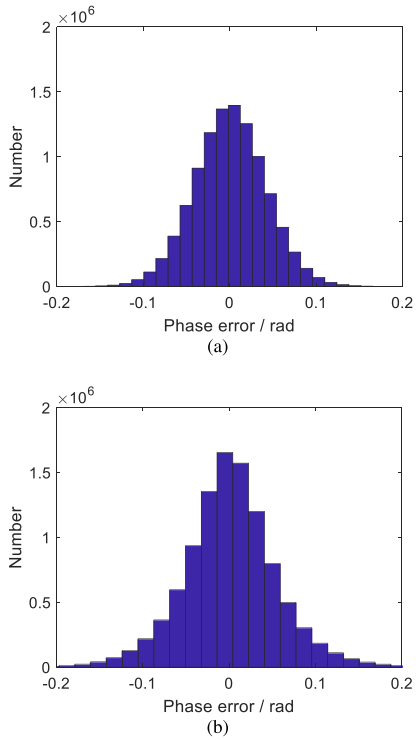

Fig. 9. Phase error. (a) Split-bandwidth processing in the echo domain. (b) Split-bandwidth processing in the image domain.

Split-bandwidth processing in the echo domain requires six times BP imaging. However, split-bandwidth processing in the image domain only requires twice BP imaging. Comparison of Fig. 9(a) with Fig. 9(b) indicates that the accuracy of the proposed method is close to the split-bandwidth in the echo domain [10]. Obviously, compared to traditional split-bandwidth in the echo domain, the proposed method is more efficient while ensuring accuracy.

V. Experimental Results

In the experiment, the real data were obtained by the airborne CSAR system independently developed by the National University of Defense Technology. The location was Shaanxi Province, China. The latitude and longitude of the CSAR imaging scene center were 35.0° N and 109.5° E, respectively. The In-CSAR data were acquired by an airborne repeat-pass L-band SAR system. The flight vehicle of the experiment is shown in Fig. 10, and the trajectory of the CSAR platform is shown in Fig. 11.

A. Result of InSAR Processing

The main parameters of the practical subaperture are given in Table II. Fig. 12 shows the imaging results of a single subaperture. The optical image of the imaging area is shown in Fig. 12(a). The BP-focusing subimage is shown in Fig. 12(b). After InSAR processing, the interferometric results of the fullband subimage are shown in Fig. 13. To obtain a reliable interferogram, the Goldstein [17] filter is used to suppress decorrelation noise. For the fullband and subband interferograms, allowing weaker

Fig. 10. Experimental flight vehicle.

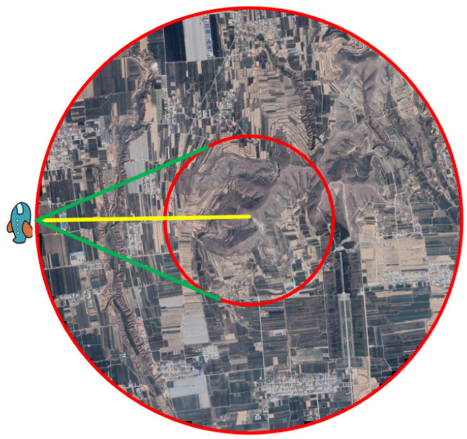

Fig. 11. Imaging scene of In-CSAR. The area of imaging is enclosed by the inner circle, and the ideal trajectory of the In-CSAR platform is represented by the outer circle.

TABLE II
Imaging Parameters of Repeat-Pass Circular InSAR

Parameter name	Values
Bandwidth-to-frequency ratio	0.16
Center of the master subaperture	$(47, -2088, 1987)$ m
Center of the slave subaperture	$(47, -2068, 1941)$ m
Equivalent velocity of the master subaperture	$(-40, -1.1, 0)$ m/s
Equivalent velocity of the slave subaperture	$(-44, 0.1, -0.35)$ m/s
Azimuth of the subaperture	1.57 rad
Integration angle of the subaperture	0.078 rad

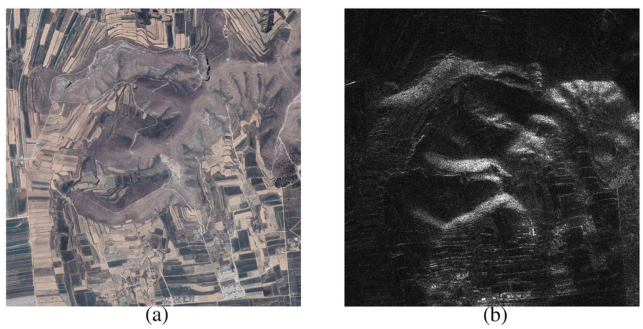

(a) (b)

Fig. 12. Imaging scene. (a) Optical image from Google Earth. (b) BP-focusing subimage.

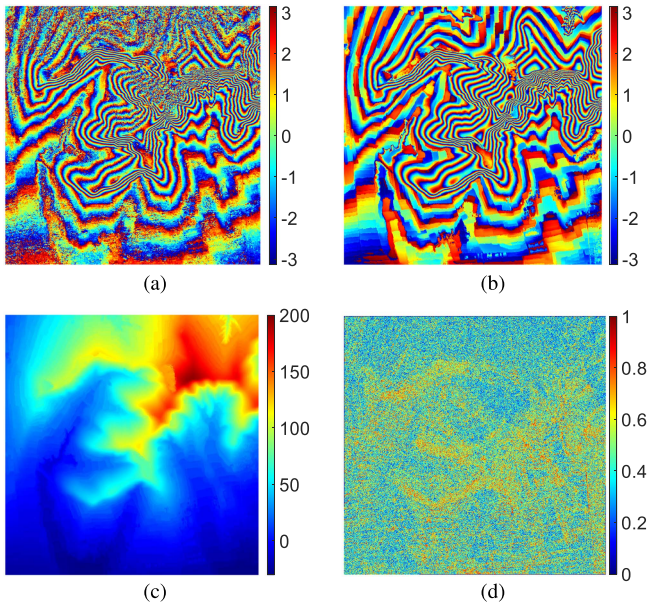

Fig. 13. Interferometric results of the fullband subimage. (a) Real terrain phase based on Goldstein filter (unit: rad). (b) Fitted terrain phase (unit: rad). (c) Reference DSM obtained by UAV (unit: m). (d) Coherence between the master and slave subimages.

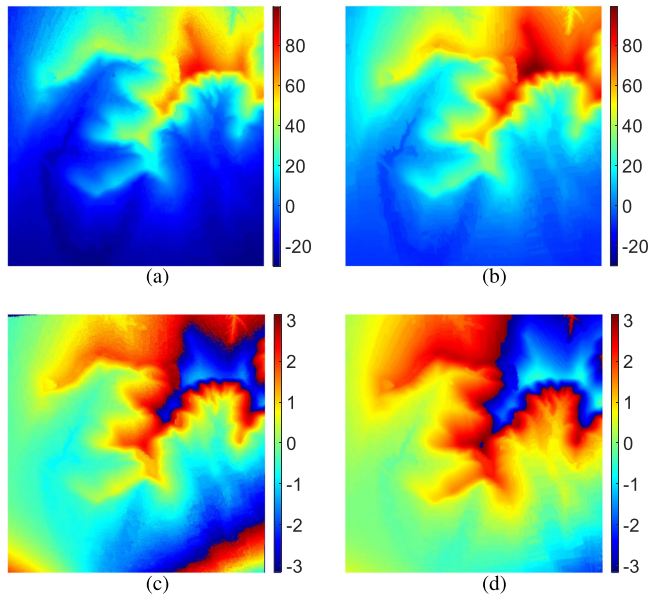

Fig. 14. Results of absolute phase estimation (unit: rad). (a) Initial unwrapped phase. (b) Absolute phase without ambiguity. (c) Initial differential interferometric phase fitted by unwrapped phase. (d) Differential interferometric phase fitted by absolute phase.

filtering to prevent the areas of high coherence (less noise) from being overfiltered. For the DDI, allowing stronger filtering in areas where there is a low coherence (high noise). Based on Goldstein filter, the terrain phase of fullband interferogram is shown in Fig. 13(a). From the optical image, most of the observation scene is mountainous without vegetation coverage. Therefore, we can obtain the digital surface model (DSM) data of the imaging scene based on unmanned aerial vehicle (UAV) optical photogrammetry technology, which serves as a reference for the accuracy of absolute phase estimation, as illustrated in Fig. 13(c). The terrain phase fitted by reference DEM is shown in Fig. 13(b). Therefore, we can see that the real and fitted terrain phases are basically the same. The coherence between the master and slave subimages is shown in Fig. 13(d).

B. *Result of Split-Bandwidth in Echo Domain*

The results of absolute phase estimation by the proposed method are shown in Fig. 14. The initial unwrapped phase is shown in Fig. 14(a). Based on the reference DEM, the absolute phase without ambiguity is shown in Fig. 14(b). After calculation, the unknown phase ambiguity is 6π. The differential interferometric phase fitted by the initial unwrapped phase is shown in Fig. 14(c). The differential interferometric phase fitted by reference DEM is shown in Fig. 14(d). Comparison of Fig. 14(c) with Fig. 14(d) indicates that the phase ambiguity can cause a significant phase offset in DDI.

The lower and upper subband interferometric phases obtained by split-bandwidth processing in the echo domain are shown in Fig. 15(a) and (b), respectively. Correspondingly, the real differential interferometric phase for the lower and upper interferograms is shown in Fig. 15(c). After absolute phase determination, the fitted differential interferometric phase is shown in Fig. 15(d). The phase error between the real and fitted differential interferometric phases is shown in Fig. 17(a). The variance of phase error is 0.0207 rad.

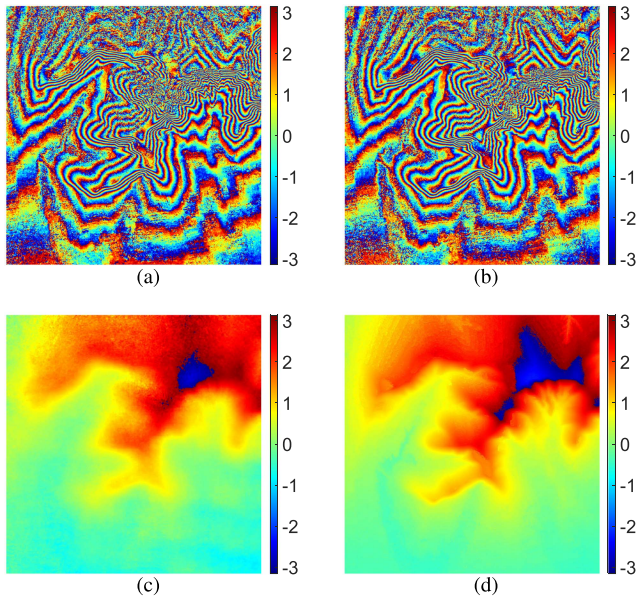

Fig. 15. Result of split-bandwidth in the echo domain (unit: rad). (a) Lower subband interferometric phase. (b) Upper subband interferometric phase. (c) Real differential interferometric phase based on Goldstein filter. (d) Fitted differential interferometric phase based on the proposed method.

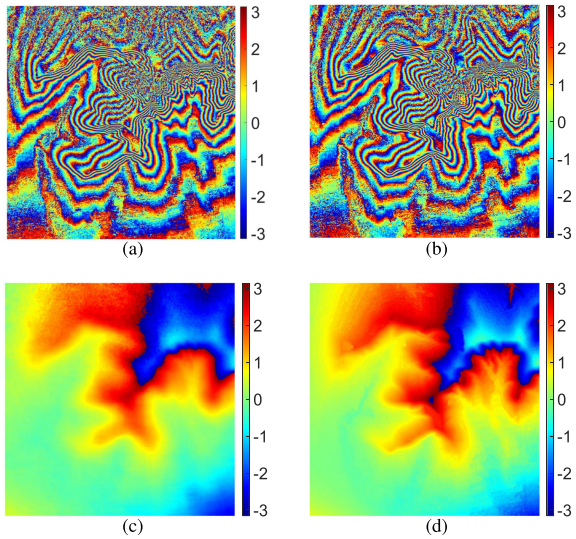

Fig. 16. Result of split-bandwidth in the BP-focusing image domain (unit: rad). (a) Lower subband interferometric phase. (b) Upper subband interferometric phase. (c) Real differential interferometric phase based on Goldstein filter. (d) Fitted differential interferometric phase based on the proposed method.

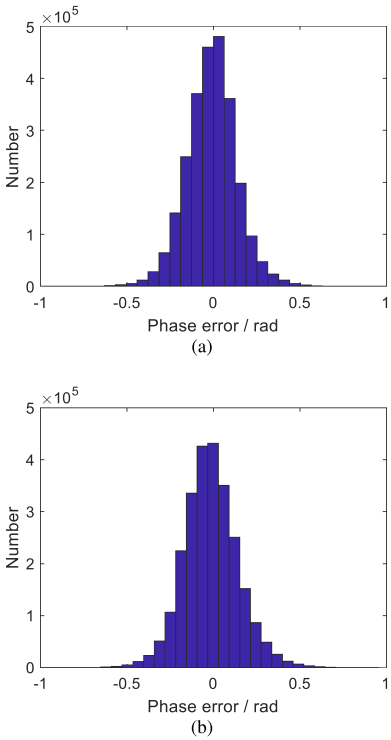

Fig. 17. Phase error. (a) Split-bandwidth processing in the echo domain. (b) Split-bandwidth processing in the image domain.

C. Result of Split-Bandwidth in BP-Focusing Image Domain

The lower and upper subband interferometric phases generated by split-bandwidth processing in the BP-focusing image domain are shown in Fig. 16(a) and (b), respectively. Correspondingly, the real differential interferometric phase obtained by split-bandwidth processing in the BP-focusing image domain is shown in Fig. 16(c). After absolute phase determination, the fitted differential interferometric phase is shown in Fig. 16(d). Comparison of Fig. 14(d) with Fig. 16(d) indicates that the proposed method can estimate phase ambiguity effectively.

The phase error between the real and fitted differential interferometric phases is shown in Fig. 17(b). The variance of phase error is 0.025 rad. Although the DDI is obtained from the image domain, our proposed method achieves a similar level of estimation accuracy as split-bandwidth processing implemented in the echo domain.

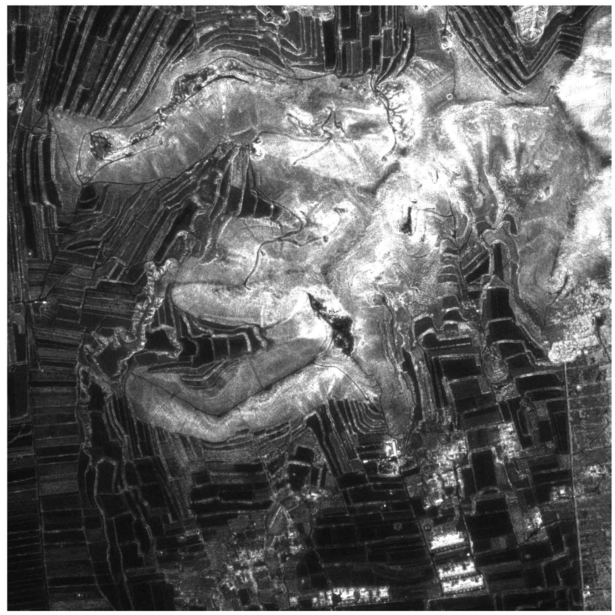

Fig. 18. Full-angle SAR image.

D. Result of the Full-Angle Processing Based on In-CSAR

To verify the effectiveness and practicability of the proposed approach, the result of the full-angle processing is obtained. First, the phase ambiguities of all subapertures are corrected and the real DEMs are obtained. Then, based on the RD model, the position offsets induced by the absence of DEMs are corrected. Finally, the BP-focusing subimages are fused to obtain a full-angle SAR image [19]. Fig. 18 shows the full-angle SAR image. Compared with the single-angle image in Fig. 12(b), the main advantage of the full-angle SAR image has lower speckle noise and more abundant textural features.

VI. Conclusion

In this article, the absolute phase estimation of In-CSAR is discussed. First, the interferometric phase expression of the BP-focusing subimage is derived. Then, based on the In-CSAR system, a novel method is presented to estimate the phase ambiguity. The proposed method can estimate the residual phase ambiguity under the conditions of the highly nonlinear and nonparallel trajectories. Finally, the effectiveness and practicability of the proposed approach is verified with the processing results of simulation and real data. Compared to traditional split-bandwidth

in the echo domain, the proposed method is more efficient while ensuring accuracy. However, the proposed method has some limitations. For example, the bandwidth-to-frequency ratio of the SAR image affects the accuracy of absolute phase estimation. In the future, for narrowband systems, absolute phase estimation based on multiangle characteristics of In-CSAR is under development.

REFERENCES

[1] K. A. C. Macedo, R. Scheiber, and A. Moreira, "An autofocus approach for residual motion errors with application to airborne repeat-pass SAR interferometry," *IEEE Trans. Geosci. Remote Sens.*, vol. 46, no. 10, pp. 3151–3162, Oct. 2008.

[2] M. Pinheiro, P. Prats, and R. Scheiber, "Tomographic 3D reconstruction from airborne circular SAR," in *Proc. IEEE Int. Geos. Remote Sens. Sym.*, 2009, pp. III-21–III-24.

[3] Y. Lin, W. Hong, W. Tan, Y. Wang, and Y. Wu, "Interferometric circular SAR method for three-dimensional imaging," *IEEE Geosci. Remote Sens. Lett.*, vol. 8, no. 6, pp. 1026–1030, Nov. 2011.

[4] Y. L. Neo, F. H. Wong, and I. Cumming, "Processing of azimuth-invariant bistatic SAR data using the range Doppler algorithm," *IEEE Trans. Geosci. Remote Sens.*, vol. 46, no. 1, pp. 14–21, Jan. 2008.

[5] B. Walker, G. Sander, M. Thompson, B. Burns, R. Fellerhoff, and D. Dubbert, "A high-resolution, four-band SAR testbed with real-time image formation," in *Proc. IEEE Int. Geos. Remote Sens. Sym.*, 1996, pp. 1881–1885.

[6] Z. Li, J. Wu, Q. Yi, Y. Huang, and J. Yang, "An omega-k imaging algorithm for translational variant bistatic SAR based on linearization theory," *IEEE Geosci. Remote Sens. Lett.*, vol. 11, no. 3, pp. 627–631, Mar. 2014.

[7] L. M. H. Ulander, H. Hellsten, and G. Stenstrom, "Synthetic-aperture radar processing using fast factorized back-projection," *IEEE Trans. Aerosp. Electron. Syst.*, vol. 39, no. 3, pp. 760–776, Jul. 2003.

[8] N. Cao et al., "Estimation of residual motion errors in airborne SAR interferometry based on time-domain backprojection and multisquint techniques," *IEEE Trans. Geosci. Remote Sens.*, vol. 56, no. 4, pp. 2397–2407, Apr. 2018.

[9] R. Brcic, M. Eineder, and R. Bamler, "Interferometric absolute phase determination with TerraSAR-X wideband SAR data," in *Proc. Radar Conf.*, 2009, pp. 1–6.

[10] S. N. Madsen, "On absolute phase determination techniques in SAR interferometry," *Proc. SPIE*, vol. 2487, pp. 393–401, 1995.

[11] S. N. Madsen, H. A. Zebker, and J. Martin, "Topographic mapping using radar interferometry: Processing techniques," *IEEE Trans. Geosci. Remote Sens.*, vol. 31, no. 1, pp. 246–256, Jan. 1993.

[12] R. Bamler and M. Eineder, "Split band interferometry versus absolute ranging with wideband SAR systems," in *Proc. IEEE Int. Geosci. Remote Sens. Symp.*, 2004, vol. 2, pp. 980–984.

[13] R. Bamler and V. M. Eineder, "Multichromatic analysis of InSAR data," *IEEE Trans. Geosci. Remote Sens.*, vol. 51, no. 9, pp. 4790–4799, Sep. 1993.

[14] T. Shi, X. Mao, A. Jakobsson, and Y. Liu, "Parametric model-based 2-D autofocus approach for general BiSAR filtered backprojection imagery," *IEEE Trans. Geosci. Remote Sens.*, vol. 60, 2022, Art. no. 5233414.

[15] R. Bamler and M. Eineder, "Accuracy of differential shift estimation by correlation and split-bandwidth interferometry for wideband and delta-k SAR systems," *IEEE Geosci. Remote Sens. Lett.*, vol. 2, no. 2, pp. 151–155, Apr. 2005.

[16] H. Q. Wang et al., "Correction of time-varyingbaseline errors based on multibaseline airborne interferometric data without high-precision DEMs," *IEEE Trans. Geosci. Remote Sens.*, vol. 59, no. 11, pp. 9307–9318, Nov. 2021.

[17] R. M. Goldstein et al., "Radar interferogram filtering for geophysical applications," *Geophys. Res. Lett.*, vol. 25, no. 21, pp. 4035–4038, 1998.

[18] Z. Xu, Z. Xie, C. Fan, and X. Huang, "Probabilistically robust radar waveform design for extended target detection," *IEEE Trans. Signal Process.*, vol. 70, pp. 4212–4224, 2022.

[19] Z. Xu, C. Fan, and X. Huang, "MIMO radar waveform design for multipath exploitation," *IEEE Trans. Signal Process.*, vol. 69, pp. 5359–5371, 2021.

[20] W. Wang, D. An, Y. Luo, and Z. Zhou, "The fundamental trajectory reconstruction results of ground moving target from single-channel CSAR geometry," *IEEE Trans. Geosci. Remote Sens.*, vol. 56, no. 10, pp. 5647–5657, Oct. 2018.

[21] D. Feng, D. An, X. Huang, and Y. Li, "A phase calibration method based on phase gradient autofocus for airborne holographic SAR imaging," *IEEE Geosci. Remote Sens. Lett.*, vol. 16, no. 12, pp. 1864–1868, Dec. 2019.

[22] L. Chen, D. An, and X. Huang, "Resolution analysis of circular synthetic aperture radar noncoherent imaging," *IEEE Trans. Instrum. Meas.*, vol. 69, no. 1, pp. 231–240, Jan. 2020.

[23] Y. Song, J. Hu, Y. Dai, T. Jin, and Z. Zhou, "Estimation and mitigation of time-variant RFI in low-frequency ultra-wideband radar," *IEEE Geosci. Remote Sens. Lett.*, vol. 15, no. 3, pp. 409–413, Mar. 2018.

[24] P. Porwal and S. K. Katiyar, "Performance evaluation of various resampling techniques on IRS imagery," in *Proc. IEEE 7th Int. Conf. Contemporary Comput.*, 2014, pp. 489–494.

[25] J. Xu, D. An, X. Huang, and P. Yi, "An efficient minimum discontinuity phase unwrapping method," *IEEE Geosci. Remote Sens. Lett.*, vol. 13, no. 5, pp. 666–670, May 2016.

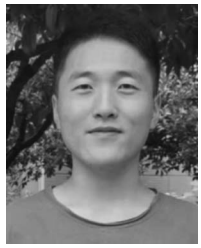

Jianpeng Li was born in Songyuan, Jilin, China. He received the B.S. degree in information and telecommunication engineering from the Harbin Institute of Technology, Harbin, China, in 2017, and the M.S. degree in electronic information science and technology, in 2020, from the National University of Defense Technology, Changsha, China, where he is currently working toward the Ph.D. degree in information and telecommunication engineering.

His research interests include SAR imaging and SAR interferometry.

Daoxiang An (Member, IEEE) received the B.S., M.S., and Ph.D. degrees in information and communication engineering from the National University of Defense Technology (NUDT), Changsha, China, in 2004, 2006, and 2011, respectively.

He is currently an Associate Professor with the College of Electronic Science and Engineering, NUDT. He has authored or coauthored more than 80 professional publications, of which more than 40 are in peer-reviewed scientific journals. His research interests include monostatic and bistatic synthetic aperture radar (SAR) imaging, 3-D SAR imaging, SAR interferometry, SAR ground moving target indication, and SAR image processing.

Yongping Song received the B.S. degree in electronic engineering and the M.S. and Ph.D. degrees in information and communication engineering from the National University of Defense Technology (NUDT), Changsha, China, in 2012, 2014, and 2019, respectively.

He is currently an Assistant Researcher with NUDT. Until 2021, he was a Lecturer with Air Force Early Warning Academy. His research interests include MIMO radar image formation, radar targets detection, and radar antijamming.

Junyi Xu was born in Shaanxi, China, in 1987. He received the B.S. degree in communication engineering from Xidian University, Xi'an, China, in 2009, and the M.S. and Ph.D. degrees in information and communication engineering from the National University of Defense Technology, Changsha, China, in 2011 and 2015, respectively.

He is currently with the Aerial Photogrammetry and Remote Sensing Group Company Ltd. of CNACG (ARSC), Xi'an, China. His research interests include phase unwrapping, algorithm design, and synthetic aperture radar interferometry signal processing and application.

Dong Feng received the B.S., M.S., and Ph.D. degrees in information and communication engineering from the National University of Defense Technology (NUDT), Changsha, China, in 2013, 2015, and 2020, respectively.

He is currently a Lecturer with NUDT. His research interests include bistatic SAR image formation, SAR interferometry, SAR tomography, and holographic SAR 3-D reconstruction.

Leping Chen (Member, IEEE) received the B.S. degree in electronic engineering and the M.S. and Ph.D. degrees in information and communication engineering from the National University of Defense Technology (NUDT), Changsha, China, in 2011, 2014, and 2018, respectively.

He is currently a Lecturer with the NUDT. His research interests include circular synthetic aperture radar image formation and high-resolution SAR image formation.

Zhimin Zhou received the B.S. degree in aeronautical radio measurement and control and the M.S. and Ph.D. degrees in information and communication engineering from the National University of Defense Technology (NUDT), Changsha, China, in 1982, 1989, and 2002, respectively.

He is currently a Professor with NUDT. His research interests include ultrawideband radar system and real-time signal processing.

Dr. Zhou is a Fellow of the Chinese Institute of Electronics, Beijing, China.